Recycling Piezoelectric Switch-Inductor Charger

Siyu Yang* and Gabriel A. Rincón-Mora

***Abstract*—Wireless microsystems that sense information about their surrounding environment can save money, energy, and lives. Piezoelectric transducers can harvest ambient vibration energy to reduce the cost and prolong lifetime of the microsystems. Outputting high power and maintaining maximum power-point is important for the charger to support functionality for the microsystems. The proposed recycling switched-inductor charger induces current at the highest voltage by keeping the piezoelectric voltage near the breakdown voltage of the CMOS charger to draw the highest power from the transducer. The charger senses when the piezoelectric voltage reaches breakdown voltage, and draws a portion of the energy to charge the battery. The direct inductor transfers allow the inductor to transfer more energy than it carries, saving ohmic loss. With a single inductor and a single stage to charge the battery across its voltage range, the proposed recycling switched-inductor charger can deliver 0.1 – 91 µW from vibrating a 15 nF piezoelectric transducer at 120 Hz with 0.1 to 10.5 V open circuit voltage gain. The prototype can output net power at 80% smaller voltage than the state of the art, can output up to 12× higher power than the lossless bridge can draw from the same transducer, and can output 76% of the theoretical maximum power a transducer can produce.**

Keywords—Piezoelectric charger, energy harvesting, recycling, CMOS, switched-inductor, maximum power-point, optimization.

I. Piezoelectric Chargers

Wireless microsystems embedded in buildings, vehicles, and even human beings can collect information about their surrounding environment to save money, energy, and lives [1]–[4]. To reduce the size of the on-board batteries and the frequency of replacing them, researchers have looked to constantly replenishing the tiny batteries with ambient energy from light, motion, and heat. Recent advances in micro-electro-mechanical systems (MEMS) technology have allowed energy harvesting transducers to shine [5]–[11].

Among the energy harvesting transducers, photovoltaic cells under direct sunlight can output the highest power [6]. However, sunlight is not always available, and when moved under artificial lights, the power level drops significantly, and even that may not be always available [6]. Piezoelectric [7], [9]–[11] transducers can harvest moderate power from vibrating motion and can be integrated into MEMS. As a result, piezoelectric harvesters can constantly charge the on-board battery to power microsystems.

The piezoelectric-powered wireless microsystem, as shown in Fig. 1, consists of the transducer, the charger that draws power from the transducer and charge the battery, and a voltage regulator to provide power to the electronic blocks of the microsystem. Because the drawn power is usually moderate to low, the charger needs to output the maximum power it can. That is why the charger needs to incorporate a maximum power point (MPP) function.

S. Yang is an Analog Design Engineer at Cirrus Logic Inc. He is the corresponding author(e-mail: jimsyyang@gatech.edu).

G. A. Rincón-Mora is with the School of Electrical and Computer Engineering, Georgia Institute of Technology, Atlanta, GA 30332-0250 USA (e-mail: rincon-mora@gatech.edu).

Piezoelectric transducers generate alternating current i_{PZ} under vibration that charges the intrinsic capacitor C_{PZ} [9], as shown in Fig. 2. Among the existing piezoelectric chargers, basic diode bridge [12]–[14] and half bridge [15] can collect some, but not all, charge created by the transducer. A portion of the charge is lost to discharging and charging piezoelectric voltage between positive and negative rectified voltages. As a result, the drawn power is low. Synchronous discharge chargers [16]–[19], on the other hand, let the piezoelectric transducer charge the capacitor open-circuit across a half cycle. At the end of the half cycle, the switched-inductor (SL) collects all the charge, which raises drawn power. However, the voltage, and as a result the drawn power, is limited by the breakdown voltage [17]. The charger also needs to sense when piezoelectric current changes direction to initiate the transfers. Although the inductor is bulky for wireless micro-sensors, it is a necessary sacrifice to significantly increase output power. Nevertheless, the system should only incorporate a single inductor to limit the overall volume.

Without a harvester, the sinusoidal piezoelectric current charges the capacitor by the open circuit voltage $\Delta v_{PZ(OC)}$ every half cycle

$$\Delta v_{PZ(OC)} = \frac{1}{C_{PZ}} \int_0^{0.5t_{VIB}} i_{PZ(PK)} \sin\left(\frac{2\pi t}{t_{VIB}}\right) dt = \frac{i_{PZ(PK)} t_{VIB}}{\pi C_{PZ}}, \quad (1)$$

where C_{PZ} is the intrinsic capacitance of the transducer, t_{VIB} is the vibration period, and $i_{PZ(PK)}$ is the peak current generated by the vibration. Because piezoelectric transducers have low mechanical to electrical coupling [13]–[28], the power that is converted into electrical domain is just a tiny portion of the overall power of the vibration. This means electrical damping is much smaller than mechanical damping, and that the power we draw from the vibration does not affect the displacement of the vibration. As a result, the higher the piezoelectric voltage, the more power the vibration generates.

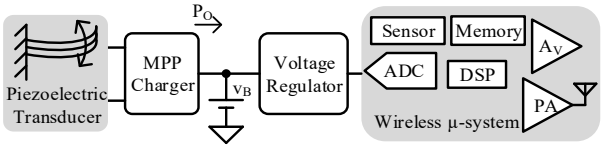

Fig. 1. Piezoelectric-powered wireless microsystem.

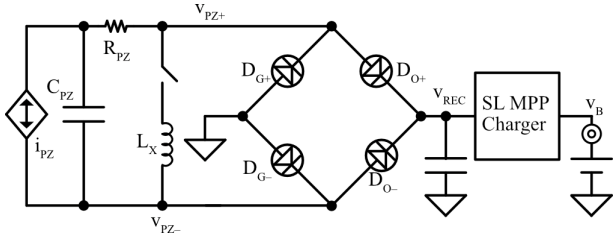

Fig. 2. Schematic of the Recycling Bridge.

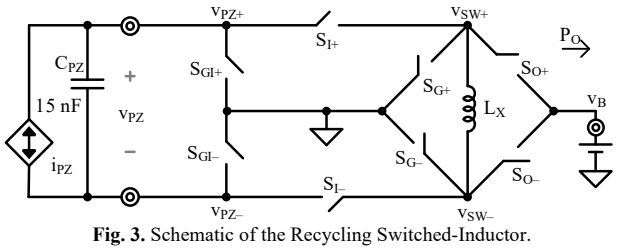

Fig. 3. Schematic of the Recycling Switched-Inductor.

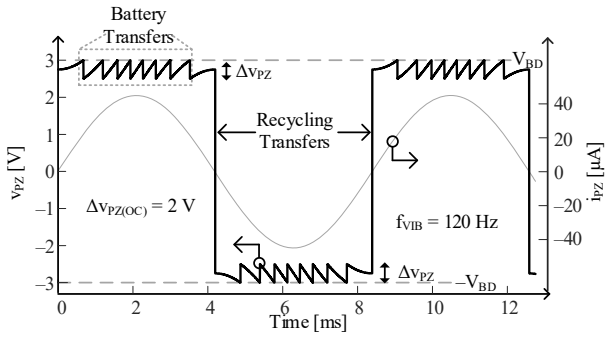

Fig. 4. Simulated piezoelectric voltage v_{PZ}.

The recycling bridge [20]–[28], shown in Fig. 2, also known as synchronous switch harvesting on inductor (SSHI), can draw the highest power possible by putting the breakdown voltage across the transducer across half cycles. The inductor L_X collects and flips the charge on C_{PZ} between half cycles. However, the recycling bridge/SSHI has to maintain the rectified voltage v_{REC} near the breakdown voltage V_{BD} of the CMOS charger to keep the drawn power high, and as a result, a second switched-inductor (SL) stage is required to maintain MPP, which is bulky and lossy.

This paper introduces a new power stage that can draw almost the same power as the recycling bridge but maintains MPP with only one inductor and one power stage. Section II discusses the operation of the recycling SL power stage. Section III details the drawn power, losses, and output power of the proposed charger. Section IV describes the implementation, and Section V assesses the power stage against the state of the art. Section VI concludes the paper.

II. Operation

A. Circuit Operation

The proposed charger, shown in Fig. 3, consists of the piezoelectric transducer, which is modeled as the current source i_{PZ} in parallel with its inherent capacitance C_{PZ}, the switch network, inductor L_X, and the battery v_B. The proposed charger differs from the recycling bridge in the state of the art in that it charges the battery at maximum power point using a single stage, instead of needing another dedicated SL stage to maintain MPP. Across vibration half cycles, i_{PZ} chargers C_{PZ}, as shown in Fig. 4. As the controller senses that $|v_{PZ}|$ reaches the maximum power point $v_{PZ(PK)}$, the charger initiates a battery-charging transfer, to collect a portion of the charger to energize the inductor, and then charge the battery. Each battery-charging transfer draws ΔE_{PZ} from C_{PZ}, and the capacitor's voltage drops by Δv_{PZ}. Because the time constant of the LC is within 10 µs, while the half cycle is across milliseconds, the transfer is nearly instantaneous. After the battery-charging transfer, the switches open, and i_{PZ} charges C_{PZ} again.

Since the charger initiates a battery-charging transfer whenever $|v_{PZ}|$ reaches $v_{PZ(PK)}$, $|v_{PZ}|$ can never go above the $v_{PZ(PK)}$. The charger connects the capacitor plate with the lower potential to ground, and the maximum power point $v_{PZ(PK)}$ to the breakdown voltage V_{BD}. This way, the system does not see a negative voltage, negating the need for a negative supply, and the system does not see a voltage higher than V_{BD} to maintain safe operation. Even if the open-circuit voltage $\Delta v_{PZ(PK)}$ goes above V_{BD} as the vibration strength increases, the voltage gain on the capacitor is broken into smaller intervals by the battery-charging transfers. Therefore, the charger can safely operate with a wider vibration range.

The sequence repeats itself, as shown in Fig. 4, until i_{PZ} reverses polarity and a half cycle ends. The charger then initiates a recycling transfer, where L_X collects charge from

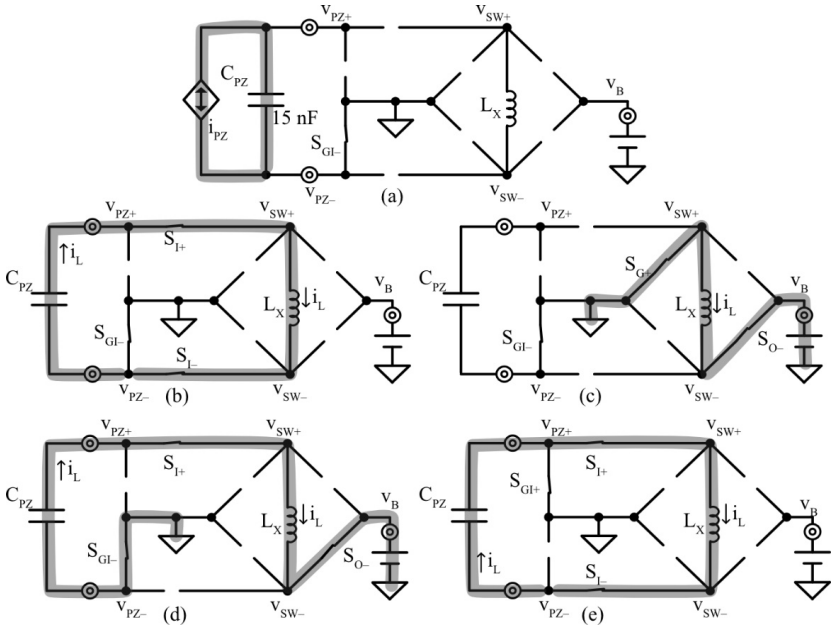

Fig. 5. Switching sequence across positive half cycle. (a) i_{PZ} charges C_{PZ}, (b) C_{PZ} energizes L_X, (c) L_X charges v_B, (d) direct transfer where C_{PZ} energizes L_X and charges v_B, and (e) L_X recycles to charge C_{PZ} to negative voltage.

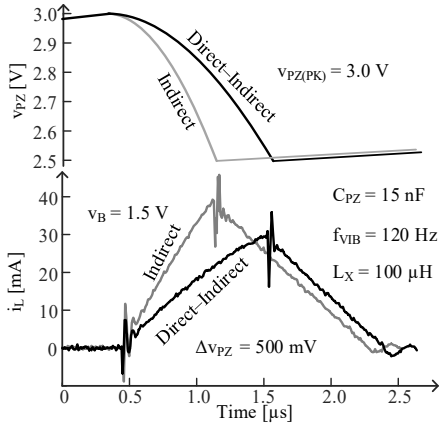

Fig. 6. Simulated v_{PZ} and Measured i_L for battery-charging transfers when Δv_{PZ} is 500 mV.

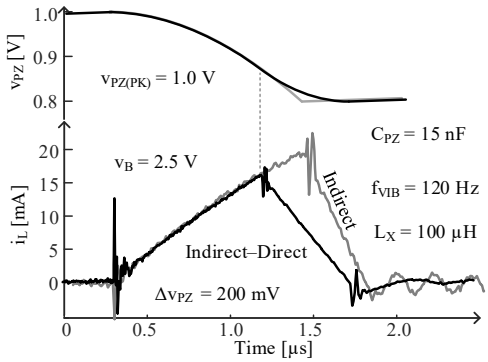

Fig. 7. Measured i_L for battery transfers when Δv_{PZ} is 200 mV.

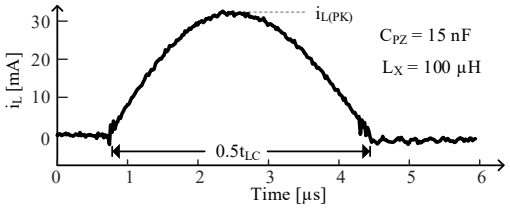

Fig. 8. Measured i_L for recycling transfers.

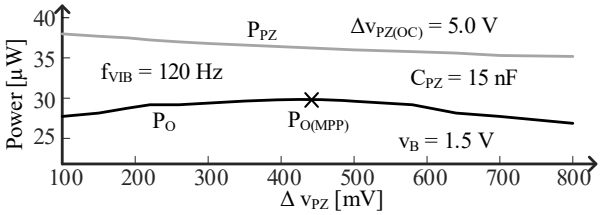

Fig. 9. Measured power across Δv_{PZ}.

C_{PZ} and puts it back to C_{PZ} in the opposite direction. This way, the charge is recycled quickly, and v_{PZ} can be near $v_{PZ(PK)}$ at the start of the next half cycle. Without losses, $|v_{PZ}|$ is always between $v_{PZ(PK)} - \Delta v_{PZ}$ and $v_{PZ(PK)}$. If the controller sets $v_{PZ(PK)}$ to breakdown voltage V_{BD}, and $\Delta v_{PZ} << V_{BD}$, the charger can draw the maximum power possible from the transducer.

B. Swiching Sequences

Figure 5 shows the switching sequence for the charger across the positive half cycle, and the gray trace highlights the current flow for each switching configuration. Since the operation and the charger is completely symmetrical, the negative half cycle is the same, but flipped vertically for the charger. When i_{PZ} charges C_{PZ} open-circuit, only S_{GI-} closes to connect v_{PZ-} to ground, as shown in Fig. 5(a). As a result, only positive voltages appear in the charger.

When a battery-charging transfer is initiated, S_{I+} and S_{I-} close for C_{PZ} to partially energize L_X, shown in Fig. 5(b). When the voltage drop on C_{PZ} reaches the targeted Δv_{PZ}, S_{I+} and S_{I-} open while S_{G+} and S_{O-} close, as shown in Fig. 5(c) so that the inductor current on L_X can charge the battery. The controller adjusts the target Δv_{PZ} by varying the energizing time. As inductor current i_L drops to 0, both switches open, and the charger goes back to the configuration in Fig. 5(a). The inductor current and capacitor voltage waveforms for a battery-charging transfer are shown with the gray traces in Figs. 6 and 7. C_{PZ} energizes L_X using Fig. 5(b) from 0.5 µs to 1.1 µs in Fig. 6, and from 0.7 µs to 1.5 µs in Fig. 7. L_X then charges the battery with Fig. 5(c) from 1.1 µs to 2.3 µs in Fig. 6, and from 1.5 µs to 1.8 µs in Fig. 7. They are labeled "indirect" transfers, because the C_{PZ} never connects directly to both the inductor and the battery.

As has been detailed in [29],[32], direct inductor transfers reduce ohmic loss. The first type of the direct transfers is the direct–indirect transfer, which starts out with connecting C_{PZ}, L_X, and v_B with S_{GI+}, S_{I+} and S_{O-}, as shown in Fig. 5(d), to energize the inductor and charging the battery directly. It's only possible when $v_{PZ(PK)}$ is higher than v_B so that i_L flows from the capacitor to the battery. This is usually the case because $v_{PZ(PK)}$ should be close to V_{BD} to increase drawn power. When the voltage drop on C_{PZ} reaches the targeted Δv_{PZ}, S_{I+} opens and S_{G+} closes i_L charges the battery with Fig. 5(c). The controller adjusts the target Δv_{PZ} by varying the energizing time. The inductor current and capacitor voltage waveforms are captured with the black traces in Fig. 6.

However, when the vibration is low, the maximum power-point can be when the $v_{PZ(PK)}$ is lower than v_B, in which case, the indirect–direct scheme can work. The inductor first energizes with switches S_{I+} and $S_{I-}$with Fig. 5(b), as v_{PZ} falls, which is depicted by the black traces from 0.5 µs to 1.2 µs in Fig. 7. The energizing stops before v_{PZ} drops by the targeted Δv_{PZ}. Then, both v_{PZ} and i_L drains to charge the battery with switches S_{GI-}, S_{I+}, and S_{O-}, using the switching configuration in Fig. 5(d). This way, C_{PZ} transfers a portion of the energy directly into the battery, allowing the inductor to transfer more energy than it carries, reducing ohmic loss.

Between half cycles, the charger senses when the i_{PZ} reaches 0 and initiate a recycling transfer to recycle the charge from C_{PZ} back to C_{PZ} in the opposite direction. C_{PZ} first drains into L_X, and when v_{PZ} is discharged to 0, i_{PZ}, still flowing in the same direction, drains into the opposite size of C_{PZ}. To do that, S_{I+} and S_{I-} are closed for the half LC oscillation to first drain the capacitor into L_X, then charge C_{PZ} in the negative direction, as the inductor current i_L in Fig. 8 shows. At the end of the positive half cycle, the switch configuration in Fig. 5(b) is used to drain C_{PZ} to energize L_X. As v_{PZ} reaches 0, ground switch S_{GI-} opens, and S_{GI+} closes to connect the top plate v_{PZ+} to ground, and L_X can charge into v_{PZ-} with the switch configuration in Fig. 5(e). As a result, during the entire operation, there is no negative voltage.

III. Output Power

A. Drawn Power

The drawn power is the integral of the instantaneous power over a vibration cycle divided by the period

$$P_{PZ} = \frac{\int_0^{t_{VIB}} i_{PZ} v_{PZ} dt}{t_{VIB}}. \quad (2)$$

Because the operation is completely symmetrical, it is equivalent to the integral over a half cycle divided by half of a vibration period

$$\begin{aligned} P_{PZ} &= \frac{\int_0^{0.5t_{VIB}} i_{PZ} v_{PZ} dt}{0.5t_{VIB}} \\ &\approx 2f_{VIB} v_{PZ(AVG)} \int_0^{0.5t_{VIB}} i_{PZ} dt \\ &\approx 2f_{VIB}(v_{PZ(PK)} - 0.5\Delta v_{PZ})(C_{PZ}\Delta v_{PZ(OC)}) \end{aligned} \quad , \quad (3)$$

where f_{VIB} is the frequency of the vibration. From (3), the drawn power is $2C_{PZ}V_{BD}\Delta v_{PZ(OC)}f_{VIB}$, which is the highest possible drawn power, when the Δv_{PZ} for each battery charging transfer is negligibly small. The drawn power drops with higher Δv_{PZ}, as shown by the gray trace in Fig. 9. Even though keeping Δv_{PZ} as small as increases drawn power, it also increases the number of battery-charging transfers N_B in each cycle, which can increase power losses.

B. Power Losses

Unfortunately drawing more power from the piezoelectric source also leads to more losses. The main source of the power loss is the equivalent series resistance (ESR) through the inductor current path, and the charge loss to switch the power switches on and off. Other losses include overlap loss, shoot-through loss, leakage, and quiescent power.

For each energy transfer, the inductor current that goes through the inductor, transducer, and the switches burns ohmic loss along its path. The ohmic loss is the root-mean-square current squared $i_{L(RMS)}^2$, times the ESR, times the duration of the transfer t_X. Therefore, the total ohmic loss is

$$\begin{aligned} P_R &= \frac{N_B E_{R(B)} + E_{R(R)}}{0.5t_{VIB}} \\ &\approx (N_B i_{L(RMS.B)}^2 t_B R_B + i_{L(RMS.R)}^2 t_R R_R)(2f_{VIB}) \end{aligned} \quad , \quad (4)$$

where N_B is the number of battery-charging transfers in a half cycle, $i_{L(RMS,B)}$ and $i_{L(RMS,R)}$ are the RMS current, R_B and R_R are the ESR, and t_B and t_R are the transfer time for the battery transfer and recycling transfer, respectively.

From (4), ohmic loss rises with the number of transfers in a vibration cycle. On the other hand, for the same vibration input, the more often the battery-charging transfers, the smaller energy packet each transfer, and the lower the inductor current and transfer time. This is why the black trace P_R first stays flat, and then rises with Δv_{PZ} in Fig. 10. The ohmic loss also rises with transfer time and RMS current of each transfer. This is why using direct transfers can reduce ohmic loss significantly, having both lower transfer current and transfer time than indirect transfers [29]. Lastly, the ohmic loss is proportional to the ESR. The resistance of the switches is inversely proportional to the width.

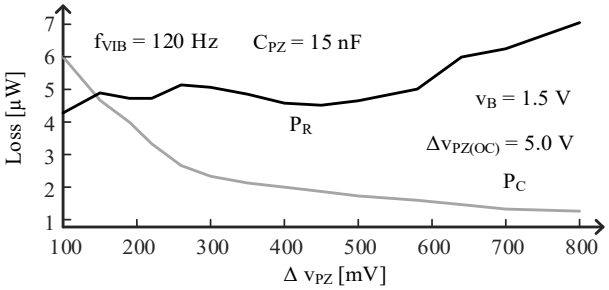

Fig. 10. Measured power losses across Δv_{PZ}.

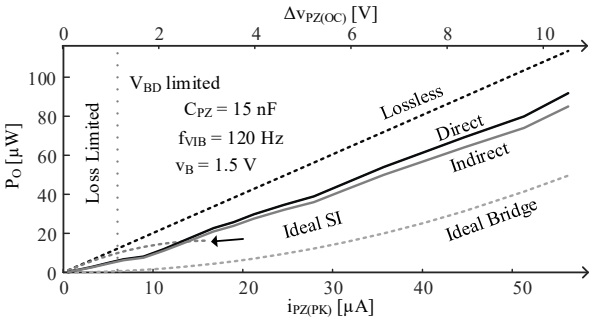

Fig. 11. Maximum output power with different vibration strength.

On the other hand, the MOSFET switches require charge to switch on and off, and in the process consumes charge loss, or switching loss. Each switch with gate capacitance C_G requires $v_{DD}C_G$ amount of charge for each switching cycle, and since it's supplied from v_{DD}, each switch consumes

$$E_C = C_G v_{DD}^2 . \quad (5)$$

Therefore, the total charge power loss P_C is

$$\begin{aligned} P_C &= \frac{N_B E_{C(B)} + E_{C(R)}}{0.5t_{VIB}} \\ &\approx (N_B C_{G,B} v_{DD}^2 + C_{G,R} v_{DD}^2)(2f_{VIB}) \end{aligned} \quad , \quad (6)$$

where $C_{G,B}$ and $C_{G,R}$ are the gate capacitance of the battery-charging transfer switches and recycling transfer switches.

The charge power loss from (6) increases with the number of battery transfers in a cycle. Therefore, P_C drops with higher Δv_{PZ}, as shown in Fig. 10 with the gray trace. The charge loss is proportional to the total gate capacitance of the switches, which rises with width. However, wider switches also result

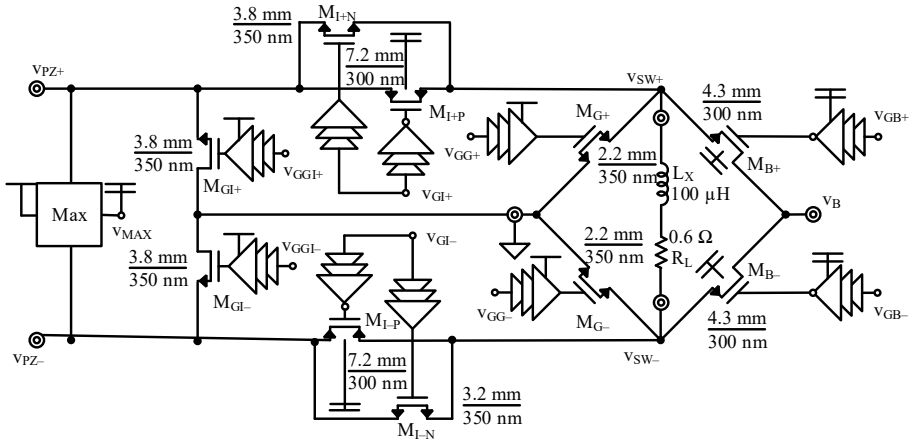

Fig. 12. Power stage implemented in 180-nm CMOS technology with 3.3-V devices.

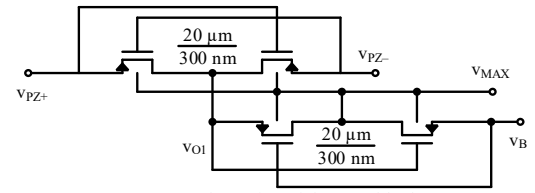

Fig. 13. Schematics of the max block.

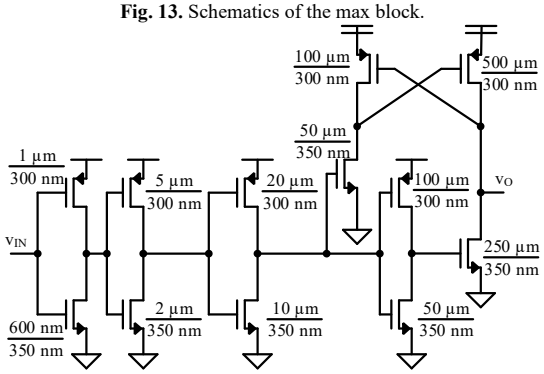

Fig. 14. Schematic of the PMOS gate drivers.

in lower resistance and lower ohmic loss. Therefore, each switch is optimally designed so that the ohmic loss balance the gate-charge loss, and the total loss is the lowest [32].

C. Output Power

The charger charges the battery N_B times every vibration cycle. For each battery-charging transfer, the energy drawn from the transducer is the energy difference on C_{PZ}

$$\Delta E_{PZ} = 0.5 C_{PZ} v_{PZ(PK)}{}^2 - 0.5 C_{PZ} (v_{PZ(PK)} - \Delta v_{PZ})^2 . \quad (7)$$

Because of the losses, the battery does not receive all the power drawn from the transducer. The output power is therefore the difference between drawn power and loss

$$P_B = \Delta E_{PZ} N_B f_{VIB} - P_R - P_C . \quad (8)$$

Figure 9 shows the output power P_O across Δv_{PZ}, and the MPP when $\Delta v_{PZ(OC)}$ is 5.0 V. As vibration rises, the number of battery-charging transfers also increases. Figure 11 depicts the maximum output power with indirect transfers (solid gray trace) and direct transfers (solid black trace). The direct scheme outputs more power because of its lower ohmic loss.

Since drawn power and losses both increase with higher $v_{PZ(PK)}$, the maximum power point is when the additional P_{PZ} starts to become lower than additional loss. When $\Delta v_{PZ(OC)}$ is higher than 1.2 V, $v_{PZ(PK)}$ is the highest at V_{BD} to maintain maximum power-point. Because V_{BD} limits how high v_{PZ} can reach, this region is breakdown limited. However, when the vibration is low, the MPP is at a smaller peak voltage $v_{PZ(PK)}$. Since additional losses overwhelms additional drawn power if $v_{PZ(PK)}$ increases, this region is loss limited, in which the charger can start outputting power with a vibration of only 0.1 V $\Delta v_{PZ(OC)}$ on the transducer.

Figure 11 also shows the maximum power a piezoelectric charger can draw with the dotted black trace label "lossless". The proposed recycling switched-inductor charger can output about 50% of the maximum power when loss limited, and can reach 76% at the maximum vibration strength.

From Fig. 11, the charger operates at or slightly lower, but never higher than the breakdown voltage V_{BD} when vibrations generate over 5 µA of peak-to-peak current on the transducer. This makes the CMOS system reliable for over 10 years of operation [30], which is longer than the expected lifespan of lithium-ion batteries. Plus, ambient vibration strength is usually so low that the charger is largely in the loss-limited MPP region. So most of the time, the highest voltage in the system is much lower than the breakdown voltage [31], further increasing its reliability.

IV. Implementation

The proposed recycling switched-inductor charger has been implemented in 0.18-µm CMOS technology with on chip power switches, max block, and gate drivers. The system is complete with Mide V22b piezoelectric transducer, a 100 µH, 0.6 Ω transfer inductor, field-programmable gate array (FPGA) that senses the piezoelectric voltage to initiate battery-charging transfers and recycling transfers and generates the control signals for the switches, and a shaker from Brüel & Kjær that can generate 0–110 µA on the transducer which translates to 0–12 V open-circuit voltage.

A. Power Stage

The power stage consists of 8 switches. Switches S_{GI+}, S_{GI-} S_{G+}, and S_{G-} are ground switches, implemented with N-type MOSFETs. Switches S_{B+} and S_{B-} are connected to v_B, and are implemented with P-type devices. This way, 0 V at the gate turns them on, and v_B or any voltage above v_B can turn them off. Switches S_{I+} and S_{I-}, on the other hand, connect two switching nodes that can both swing from 0 to the breakdown voltage. Therefore a transmission gate, with an NMOS and a PMOS in parallel, is implemented. All the switches are shown in Fig. 12. Note that some of the MOSFETs have two arrows on its symbol. This is because the current can flow in either direction in different transfers, and the source, which the arrow denotes, can be at either side of the NMOS. Otherwise they are the standard 3.3-V devices.

Bulk Connection: When an NMOS (PMOS) is turned off and its bulk voltage is a diode voltage below (above) its source voltage, the body diode turns on and conducts unwanted current. For NMOS switches, since there is no negative voltage in the system, all the NMOS can have their bulk connected to ground, and the body diodes will not turn on. The PMOS switches, however, are different because the piezoelectric voltage and the battery voltage can vary between 0 and V_{BD}. Therefore, v_{PZ} can be higher or lower than v_B. To avoid leakage, the bulk of the PMOS switches have to connect to the highest voltage. Therefore, a max block is needed to select the highest of the three voltages among v_{PZ+}, v_{PZ-}, and v_B to feed the bulk and the gate drivers.

Design: The MOSFET switches should have minimum channel length to reduce on resistance and gate capacitance. Even though the chip is fabricated in 0.18-µm CMOS technology, the 3.3 V devices have 350 nm and 300 nm minimum channel length for NMOS and PMOS respectively.

The channel widths of the switches are carefully designed to reduce losses. Since the on resistance is inversely proportional to the channel width yet the gate capacitance is proportional to it, there is an optimum width for each switch such that the sum of the ohmic loss and gate charge power loss is the lowest [32]. Specifically, the total loss on a switch is the lowest when the ohmic loss is the same as the gate charge power loss, which has been proven in [32]. The switches are optimized so that each switch is the least lossy.

B. Max Block

As discussed in the previous sub-section, the max block outputs the highest voltage among its three inputs. Two cross-

coupled PMOS pairs can accomplish this function, similar to [18]. Each cross-coupled PMOS pair connects the middle node to the higher input if it's at least a threshold higher than the other input. As Fig. 13 shows, v_{O1} is connected to the higher of v_{PZ+} and v_{PZ-}, and v_{MAX} is connected to the higher voltage of v_{O1} and v_B. Since v_{MAX} is the highest voltage of all, the bulks of the PMOS are connected to it.

C. Drivers

The switches require gate drivers to turn them on and off quickly. An inverter chain with each stage 2.72× larger than the previous stage can produce the shortest delay. However, increasing the number of the stages results in larger switching and shoot-through losses. An inverter chain in which each stage is 5× to 10× larger than the previous stage is used.

The NMOS switches can be turned on with v_B and turned off with ground. The PMOS switches, on the other hand, must be turned on with ground and turned off with v_{MAX}. Therefore, a level shifter is needed between the signals from the controller and the gate. As Fig. 14 shows, the level shifter with cross-coupled PMOS is used as the last stage of the inverter chain, to minimize the loss on the gate driver.

D. Prototype

The prototype was fabricated in 0.18-µm CMOS technology with an active area of 500 × 550 µm^2, as shown in Fig. 15. It has a 16-pin small-outline integrated circuit (SOIC) package, and, along with the 10 × 50 × 1 mm^3 piezoelectric transducer and 5 × 5 × 3 mm^3, 100 µH, 0.6 Ω inductor, has been soldered onto a printed circuit board (PCB) in Fig. 16 to test its functionality. Figure 17 shows the measured piezoelectric voltage waveform. It differs from Fig. 4 in that the losses occurred in the recycling transfers resulted in the voltage at the start of the half cycle being lower than that at the end. As a result, the drawn power is slightly reduced, and the number of battery-charging transfers in a cycle N_B also drops.

The FPGA controller, the DE1-SoC Development Kit, which is absent in Fig. 3, senses when v_{PZ} reaches the desired $v_{PZ(PK)}$ to initiate a battery-charging transfer. The FPGA is set to indirect mode, direct-indirect mode, or indirect-direct mode. The FPGA then adjusts the energizing time to control the voltage drop Δv_{PZ} for each battery-charging transfer in each mode described in Section II.B. The drain time is set when inductor current reaches 0. The FPGA also senses when half cycles end to initiate recycling transfers by comparing v_{PZ} against its previous value, and senses when $|v_{PZ}|$ starts to drop. Even though the FPGA consumes more power than the controllers in the state of the arts' 0.5-1.5 µW [15], [20]–[21], they perform similar tasks. Therefore, 1.5 µW is subtracted from the measured output power for comparisons.

The measured battery charging capability is shown in Fig. 18. A 270-nF capacitor is used to highlight the charging profile, while normally the battery has much larger capacitance to maintain functionality for the wireless microsystem. The battery charging is intermittent because the after each recycling transfer, it takes some time for the piezoelectric voltage to reach the breakdown voltage again, as shown in Fig. 17. A recycling transfer occurs at 3 ms in Fig. 18, and the transducer charges C_{PZ} to V_{BD} at 5.5 ms to start battery transfers. It shows that with each battery transfer, the battery receives energy throughout the range of 0.5 V to 2.5 V. As a result, the need for an extra maximum power-point charging stage is eliminated.

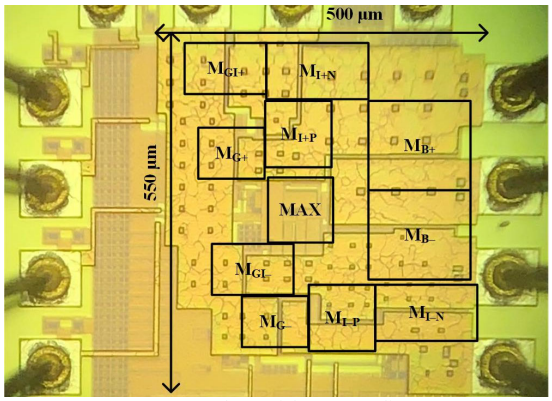

Fig. 15. Photo of the CMOS die.

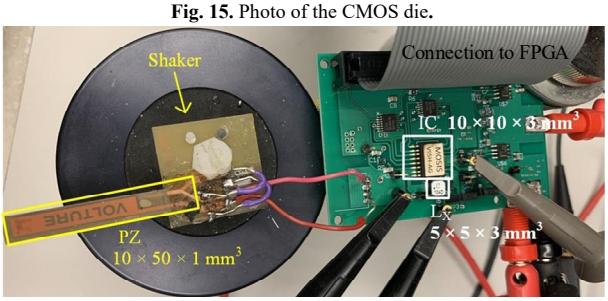

Fig. 16. Photo of the testing setup.

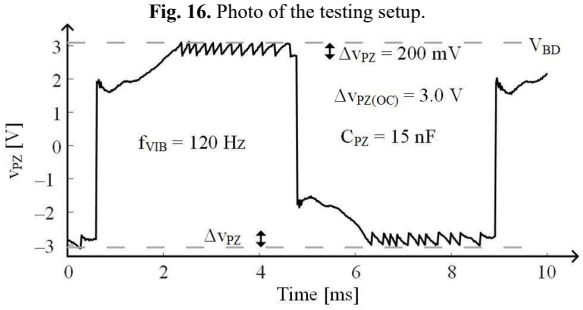

Fig.17. Measurement piezoelectric voltage v_{PZ}.

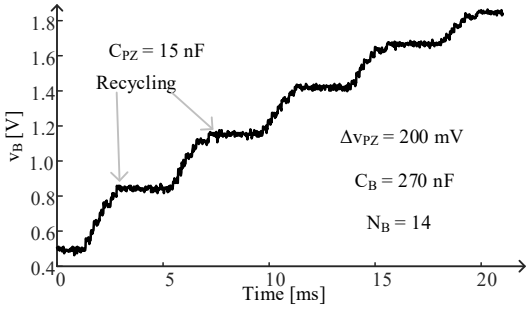

Fig. 18. Measurement of the battery charging with a 270-nF capacitor.

V. Assessment

A. Metric

The focus of this research is on the MPP charger, not the transducer. Therefore, comparing performance without normalizing the transducer or vibration is unfair. The parameters that the transducer and vibration contribute to the maximum output power are intrinsic capacitance C_{PZ}, series resistance R_{PZ}, peak piezoelectric current $i_{PZ(PK)}$, and vibration frequency f_{VIB}. Since from (1), C_{PZ}, $i_{PZ(PK)}$, and f_{VIB} determine the open-circuit voltage gain $\Delta v_{PZ(OC)}$, $\Delta v_{PZ(OC)}$ is used to obtain a metric to compare chargers.

The ideal bridge [12]–[14], at maximum power-point, can collect half of the charge generated by the vibration $0.5C_{PZ}\Delta v_{PZ(OC)}$, at a quarter of the open-circuit voltage

$0.25\Delta v_{PZ(OC)}$, twice per vibration period T_{VIB}. As a result, the maximum power they can draw is

$$P_{BRG(IDEAL)} = 0.25 C_{PZ} \Delta v_{PZ(OC)}{}^2 f_{VIB}. \quad (9)$$

This expression contains all the independent components that are related to the transducer and vibration and excludes all the variables that a circuit designer control. Therefore, it is a good parameter to normalize the effect of the transducer. The ideal power is shown with the gray dotted trace in Fig. 11.

In this light, maximum output power index $\eta_{O(MPP)}$ is how much more power a certain charger can output to the battery compared to what the ideal bridge can draw

$$\eta_{O(MPP)} = \frac{P_{O(MPP)}}{P_{BRG(IDEAL)}}. \quad (10)$$

This metric normalizes the transducer and vibration and can be used to compare chargers.

Another ideal power stage, the ideal recycling charger, can produce another normalized power index, especially if breakdown voltage limits the output power of a charger. The maximum power of a lossless recycling charger is $2C_{PZ}V_{BD}\Delta v_{PZ(OC)}f_{VIB}$. The percentage of that ideal power that the charger can output to the battery is

$$\eta_{O(BD)} = \frac{P_{O(MPP)}}{2C_{PZ}V_{BD}\Delta v_{PZ(OC)}f_{VIB}}. \quad (11)$$

This normalizes the transducer, vibration, and the breakdown voltage, can be used to compare recycling chargers.

B. Comparison

The state of the art has been categorized and summarized in Table I. Non-ideal diode bridges and half bridges can draw less than P_{IDEAL}. As a result, the power index for the basic bridge is well under 1. The switched-inductor power stage improves upon the basic bridges by collecting all the charge. It can draw as much as four times higher power than the ideal bridge can draw. Pre-charging further increases the voltage the charge is generated at. Even though the power stage consumes more ohmic and charge loss, the output power index can be as high as 6.8× [17].

The recycling bridges can draw the highest power, because the piezoelectric voltage can always be the highest at near V_{BD}. However, it requires a MPP charger to regulate the rectified voltage at the breakdown voltage, and the most efficient way to accomplish that is to use another switched-inductor power stage. A two-inductor solution is not ideal for the microsystem application, and because of the added losses, the output power index is still only about 6.8×.

C. This Technology

The proposed recycling switched-inductor charger also draws high power because v_{PZ} is near the breakdown voltage across the half cycle. Moreover, it does not require a second stage or a second inductor to achieve maximum power-point, since it can charge the battery directly across its range. By dividing the open circuit voltage gain $v_{PZ(OC)}$ into smaller pieces, the proposed charger can withstand wider input vibration strength range. Therefore, it can output up to 85 µW from 10.5 V open circuit voltage gain from a 120 Hz vibration on a 15-nF piezoelectric capacitance. Using direct transfers further reduces the ohmic losses. The output power can be up to 91 µW with an output power index of 12×, outperforming the state of the arts despite the lowest breakdown limit.

Another significant advantage of the proposed power stage is that it can output net power when the vibration is very low. The charger starts outputting power when the vibration only generates 0.1 V peak to peak open-circuit voltage on the capacitance, which is five times lower that the state of the art. This is because all the losses can scale with input power. The 12× power index is achieved when the vibration is low: it outputs 100 nW net power with 0.1 V $\Delta v_{PZ(OC)}$, which corresponds with 8 nW of P_{IDEAL}. Even though the proposed power stage has the greatest number of switches, because of the low breakdown voltage and the low ohmic loss thanks to direct transfers, the active area is still among the lowest of the state of the art. With a wider input range, the charger can charge the battery more frequently. The drawbacks of this technology are the lack of integrated MPP controller, and the inability of startup without an existing battery voltage.

VI. Conclusitons

The proposed recycling switched-inductor charger can deliver 0.1 – 91 µW from vibrating a 15 nF piezoelectric transducer at 120 Hz with 0.1 to 10.5 V open circuit voltage $\Delta v_{PZ(OC)}$. The prototype can output net power at 80% smaller vibration strength than the state of the art, and up to 12× higher power

TABLE I. Relative Performance

	JSSC [19]	**JSSC [15]**	**TPE [17]**	**JSSC [21]**	**TCAS-I [20]**	**JSSC [23]**	**JSSC [28]**	**This Work**
Power Stage	Diode Bridge	SL Half Bridge	SL Bridge	Recycling SL Diode Bridge				Recycling SL
L_{MIN}	1 µm	0.18 µm	0.82–1.2 µm	350 nm	250 nm	350 nm	130 nm	0.3–0.35 µm
V_{BD}		15 V	5.5 V			5 V		3.3 V
Si. Area	4.25 mm²	2.3 mm²	0.25 mm²	9.0 mm²	0.75 mm²	0.54 mm²	0.53 mm²	0.26 mm²
L_X		330 µH	330 µH	1000 µH	220 µH	3400 µH	47 µH	100 µH
C_{PZ}	12 nF	15 nF	17 nF	5.2 µF	19 nF	9.6 nF	14 nF	15 nF
f_{VIB}	225 Hz	143 Hz	120 Hz	82 Hz	144 Hz	230 Hz	441 Hz	120 Hz
$\Delta v_{PZ(OC)}$	4.8 V	1.22–5.24 V	0.50–5.5 V	1.0–12 V	9.8 V	≥ 1.34 V	3 – 4 V	0.15– 10.5 V
P_{IDEAL}	15.6 µW	0.80–15.1 µW	0.13–15 µW	0.11–15.3 mW	65.7 µW	≥0.99 µW		0.008 – 41 µW
P_{PZ}	8.2 µW	7–78 µW	1.2–55 µW					0.2 – 120 µW
$P_{O(MPP)}$	7.5 µW	2.1–52.5 µW	0.70–49 µW	1.7 mW	136 µW	5–410 µW	40.6 µW	0.1 – 91 µW
P_Q		0.5 µW	Off Chip	777 nW	1.5 µW			Off Chip
$\eta_{O(MPP)}$	48 %	2.6×–3.5×	3.2×–6.8×		2.1×	3.1×–6.8×	4.48×	2.5 – 12×
$\eta_{O(BD)}$			Up to 14%*	39%*		Up to 63%*		Up to 76%
Components	4 FETs MPP Buffer	L_X, 2 FETs	L_X, 4 FETs	L_X, 6 FETs MPP Buffer	L_X, 4 FETs MPP Buffer	L_X, 6 FETs MPP Buffer	L_X,10 FETs MPP Buffer	L_X,10 FETs

* Calculated from data points.

than the lossless bridge can draw from the same transducer. The charger can output up to 76% of the theoretical maximum power a piezoelectric transducer can draw with 3.3 V breakdown voltage. It is possible because the single-stage charger can charge the battery at its maximum power-point without another MPP charger stage which is lossy. The charger draws the maximum power possible by keeping the piezoelectric voltage near the V_{BD}, maximizing the voltage at which the transducer induces the current. The charger is further optimized with direct transfers, allowing the inductor to transfer more power than it carries, further reducing ohmic loss. With optimized power switches, the charger outputs the most power from the piezoelectric transducers to replenish the on-board battery across its voltage range. This way, the battery can power the wireless microsystems with a longer lifetime and wider functionality to save money, energy, and lives.

ACKNOWLEDGMENT

The authors would like to thank Texas Instruments for sponsoring this research and Dr. Orlando Lazaro, Dr. Andres Blanco, and Dr. Jeff Morroni for their advice and support.

Data sharing is not applicable to this article as no datasets were generated or analyzed during the current study.

REFERENCES

[1] S. Roundy, P. Wright, and J. Rabaey, "A study of low level vibrations as a power source for wireless sensor nodes," *Computer Communications*, vol. 26, no. 11, pp. 1131–1144, July 2003.

[2] F. Goodarzy, E. Skafidas, and S. Bambini, "Feasibility of energy-autonomous wireless microsensors for biomedical applications: powering and communication," *IEEE Reviews in Biomedical Engineering*, vol. 8, pp. 17–29, August 2015.

[3] M. Belleville, H. Fanet, P. Fiorini, P. Nicole, M.J.M. Pelgrom, C. Piguet, R. Hahm, C. Van Hoof, R. Vullers, M. Tartagni, and E. Cantatore, "Energy autonomous sensor systems: towards a ubiquitous sensor technology," *Microelectronics Journa*l, vol. 41, pp. 740–745, February 2010.

[4] R.J.M. Vullers, R. van Schaijk, I. Doms, C. van Hoof, and R. Mertens, "Micropower energy harvesting," *Solid-State Electronics*, vol. 53, no. 7, pp. 684–693, July 2009.

[5] J.A. Paradiso and T. Starner, "Energy scavenging for mobile and wireless electronics," *IEEE Pervasive Comput*, vol. 4, no. 1, pp. 18–27, 2005.

[6] Y. Hung, M. Cai, J. Chen, H. Su, P. Jen, P. Chen , C. Shih, and T. Chang, "High-Voltage Backside-Illuminated CMOS Photovoltaic Module for Powering Implantable Temperature Sensors," *IEEE Journal of Photovoltaics*, vol. 8, no. 1, pp. 342-347, Jan. 2018.

[7] S.P. Beeby, M.J. Tudor, and N.M. White, "Energy harvesting vibration sources for microsystems applications," *Measurement Science and Technology*, vol. 17, no. 12, pp. 175–195, December 2006.

[8] H. Liu, Y. Qian, N. Wang and C. Lee, "An in-plane approximated nonlinear MEMS electromagnetic energy harvester," *J. Micro-electromechanical Systems*, vol. 23, no. 3, pp. 740-749, June 2014.

[9] P.D. Mitcheson, E.M. Yeatman, G.K. Rao, A.S. Holmes, and T.C. Green, "Energy harvesting from human and machine motion for wireless electronic devices," *in Proceedings of the IEEE*, vol. 96, no. 9, pp. 1457–1486, Sept. 2008.

[10] M. Renaud, K. Karakaya, T. Sterken, P. Fiorini, C. Van Hoof, and R. Puers, "Fabrication, modelling and characterization of MEMS piezoelectric vibration harvesters," *Sensors and Actuators A: Physical*, vol. 145–146, pp. 380–386, July-Aug. 2008.

[11] G.A. Rincón-Mora and S. Yang, "Tiny piezoelectric harvesters: Principles, constraints, and power conversion," *IEEE Transactions on Circuits and Systems I*, vol. 63, no. 5, pp. 639–649, May 2016.

[12] G. Ottman, H. Hofmann, A. Bhatt, and G. Lesieutre, "Adaptive Piezoelectric Energy harvesting Circuit for Wireless Remote Power Supply," *IEEE Trans. on Power Electronics*, vol. 17, no. 5, pp. 669–676, May. 2002.

[13] C. Lu, C.Y. Tsui, and W.H. Ki, "Vibration energy scavenging system with maximum power tracking for micropower applications," *IEEE Trans. Very Large Scale Integr. (VLSI) Syst* , vol. 19, no. 11, pp. 2109–2119, Nov. 2011.

[14] A. Tabesh and l.C. Grechette, "A Low-Power Stand-Alone Adaptive Circuit for Harvesting Energy from a Piezoelectric Micropower Generator", *IEEE Trans. Industrial Electronics*, vol. 57, no. 3, pp. 840–849, Mar. 2010.

[15] D. Kwon and G.A. Rincón-Mora, "A single-inductor 0.35-μm CMOS energy-investing piezoelectric harvester," *IEEE J. Solid-State Circuits*, vol. 49, no. 10. pp. 2277–2291, Oct. 2014.

[16] I.M. Darmayuda, Y. Gao, M.T. Tan, S.J. Cheng, Y. Zheng, M. Je, and C.H. Heng, "A Self-Powered Power Conditioning IC for Piezoelectric Energy Harvesting from Short-Duration Vibrations", *IEEE Trans. Circuits Syst. II, Exp. Briefs*, vol. 59, no. 9, pp. 578–582, Sep. 2012.

[17] S. Yang and G.A. Rincón-Mora, "Energy harvesting piezoelectric-powered CMOS series switched-inductor bridge," *IEEE Transactions on Power Electronics*, vol. 34, no. 7, pp. 6489–6497, July 2019.

[18] J. Dicken, P.D. Mitcheson, I. Stoianov, and E.M. Yeatman, "Increased power output from piezoelectric energy harvesters by pre-biasing," in *Proc. PowerMEMS*, pp. 75–78, Dec. 2009.

[19] Y.K. Ramadass and A.P. Chandrakasan, "An efficient piezoelectric energy harvesting interface circuit using a bias-flip rectifier and shared inductor," *IEEE J. Solid-State Circuits*, vol. 45, no. 1, pp. 189–204, Jan. 2010.

[20] L. Wu, X. Do, S. LEE and D.S. Ha, "A self-powered and optimal SSHI circuit integrated with an active rectifier for piezoelectric energy harvesting," *IEEE Transactions on Circuits and Systems I: Regular Papers*, vol. 64, no. 3, pp. 537–549, March 2017.

[21] S. Du, Y. Jia, C.D. Do, and A.A. Seshia, "An efficient SSHI interface with increased input range for piezoelectric energy harvesting under variable conditions," *IEEE J. Solid-State Circuits*, vol. 51, no. 11, pp. 2729–2742, Nov. 2016.

[22] D.A. Sanchez, J. Leicht, F. Hagedorn, E. Jodka, E. Fazel, and Y. Manoli, "A parallel-SSHI rectifier for piezoelectric energy harvesting of periodic and shock excitations," *IEEE J. Solid-State Circuits*, vol. 51, no. 12, pp. 2867–2879, Dec. 2016.

[23] S. Javvaji, V. Singhal, V. Menezes, R. Chauhan, and Shanthi Pavan, "Analysis and design of a multi-step bias-flip rectifier for piezoelectric energy harvesting," *IEEE J. Solid-State Circuits*, vol. 54, no. 9, pp. 2590–2600, Sept. 2019.

[24] S. Du, Y. Jia, C. Zhao, G.A.J. Amararunta, and A.A. Seshia, "A nail-size piezoelectric energy harvesting system integrating a MEMS transducer and a CMOS SSHI circuit," *IEEE Sensor Journal*, vol. 20, no. 1, pp. 277–285, Jan. 2020.

[25] D. Guyomar, A. Badel, E. Lefeuvre and C. Richard, "Toward energy harvesting using active materials and conversion improvement by nonlinear processing," *IEEE Transactions on Ultrasonics, Ferroelectrics, and Frequency Control*, vol. 52, no. 4, pp. 584-595, April 2005.

[26] E. Lefeuvre, A. Badel, C. Richard, L. Petit, and D. Guyomar, "A comparison between several vibration-powered piezoelectric generators for standalone systems," *Sensors Actuators A*, vol. 126, pp. 405–416, 2006.

[27] A. Brenes, A. Morel, J. Juillard, E. Lefeuvre, and A. Badel, "Maximum power point of piezoelectric energy harvesters: a review of optimality condition for electrical tuning," *Smart Material and Structures*, vol. 29, no. 3, pp. 033001 – 033033, March 2020.

[28] Z. Chen, M. Law, P. Mak, W. Ki and R. P. Martins, "Fully integrated inductor-less flipping-capacitor rectifier for piezoelectric energy harvesting," *IEEE J. Solid-State Circuits*, vol. 52, no. 12, pp. 3168-3180, Dec. 2017.

[29] S. Yang and G.A. Rincón-Mora, "Least lossy piezoelectric energy-harvesting charger," *in Proceedings of 2019 IEEE 62nd International Midwest Symposium on Circuits and Systems (MWSCAS)*, Dallas, TX, USA, 2019, pp. 275-27.

[30] E. Maricau and G. Georges, "Transistor aging-induced degradation of analog circuits: Impact analysis and design guidelines," *2011 Proceedings of the ESSCIRC*, IEEE, 2011

[31] H. Wenzel and D. Pichler. *Ambient vibration monitoring*. John Wiley & Sons, 2005.

[32] S. Yang and G.A. Rincón-Mora, "Efficient Power Transfers in Piezoelectric Energy-Harvesting Switched-Inductor Chargers," in *IEEE Transactions on Circuits and Systems II: Express Briefs,* vol. 68, no.4, pp. 1248-1252, April 2021